Nanoscale

PAPER

View Article Online
View Journal | View Issue

Cite this: *Nanoscale*, 2017, **9**, 4013

Chemiresistive properties regulated by nanoscale curvature in molecularly-linked nanoparticle composite assembly†

Han-Wen Cheng,*[a,b] Shan Yan,[b] Li Han,‡[b] Yong Chen,[a] Ning Kang,[b] Zakiya Skeete,[b] Jin Luo[b] and Chuan-Jian Zhong*[b]

Received 1st December 2016,
Accepted 18th February 2017

DOI: 10.1039/c6nr09315a

rsc.li/nanoscale

Interparticle spatial properties influence the electrical and functional properties of nanoparticle-structured assemblies. This report describes the nanoscale curvature-induced change in chemiresistive properties of molecularly-linked assemblies of gold nanoparticles on multiwalled carbon nanotubes, which are exploited for sensitive detection of volatile organic compounds. In addition to using linking/capping molecules to define interparticle spatial distances, the nanoscale curvature radius of the carbon nanotubes provides intriguing tunability of the interparticle spatial properties to influence electrical properties, which contrast with those observed for nanoparticle thin films assembled directly on chemiresistor devices. The electrical characteristics of the nanoparticle–nanotube composite give positive response profiles for the vapor molecules that are distinctively different to those observed for conventional nanoparticle thin-film assemblies. The dominant effect of electron coupling on overall chemiresistive properties is shown in relation to that of nanoscale curvature radius on the nanoparticle thin-film sensing properties. Sensing data are also further assessed in correlation with the solubility parameters of the vapor molecule. These findings have significant implications for the design of sensitive interfaces with nanocomposite-structured sensing materials and microfabricated chemiresistor devices.

1. Introduction

The assembly of monolayer-capped or molecularly linked metal nanoparticles as sensing thin films is an important pathway for tuning electrical properties in the construction of highly sensitive interfaces for various sensor applications.[1–15] In addition to electrical tunability, high surface area is important in enabling high-performance sensor interfaces. Since our demonstration of the facial assembly of gold nanoparticles on carbon nanotubes (CNTs) through van der Waals interactions,[16] more studies have reported combinations of nanoparticles and CNTs through various interactions, exploring their high specific surface area and unique electrical properties. As electronic materials, CNTs feature p-type semiconductor characteristics,[17] and are conductive or semiconductive along the tubes and quantized across the tubes in single-walled and multiwalled CNTs (SWCNTs and MWCNTs). The unique physical and chemical properties of CNTs allow electronic conductivity tuning, by adjusting nanotube diameters and surface properties, for catalysis, sensors, and biosensors. Studies of the electrical properties of CNTs towards sensing applications have focused on exploring p-type semiconducting properties in response to electron injection or donation into nanomaterials.[18] Metal/CNTs interact with oxidizing gases, such as NO_2, or electron acceptors, by removing electrons and injecting holes into them, which lowers the Fermi energy level and increases conductivity. In contrast, they interact with reducing gases, such as CH_4, SO_2, and NH_3, or electron donors, by injecting electrons into them, which decreases the charge-carrier concentration and conductivity.[17] Using nanoparticles assembled on CNTs by van der Waals and electrostatic interactions, studies have focused on electrochemical detection,[19] including Pd/SWCNTs for nitrite oxidation,[20] SbNP-MWCNTs for heavy metal (Pb^{2+} and Cd^{2+}) detection,[21] positively-charged AuNP–SWNT nanohybrids for DNA detection,[22] Au–PtNP/MWCNTs for cefotaxime determination,[23] CNT@SnO_2/NP hybrids for H_2O_2 detection,[24] and AuNP/MWCNTs for glucose biosensing.[25] While the electron donating/accepting properties of isolated SWCNTS or their films have been studied, using O_2 and NO_2-induced changes

[a]*School of Chemical and Environmental Engineering, Shanghai Institute of Technology, Shanghai 201418, China. E-mail: hwcheng@sit.edu.cn*
[b]*Department of Chemistry, State University of New York at Binghamton, Binghamton, NY13902, USA. E-mail: cjzhong@binghamton.edu*

†Electronic supplementary information (ESI) available: Additional theoretical and experimental data. See DOI: 10.1039/c6nr09315a

‡Current address: RTI International, Research Triangle Park, NC, 27709, USA.

in electrical conductivity of the semiconducting CNTs,[26] and detecting volatile organic compounds (VOCs) using gold nanoparticles on amine-modified multiwalled CNTs on chemiresistor,[27] the molecular interactions and sensing mechanisms remain unclear.

Understanding these interactions is important for exploring NP–CNT systems for sensor or biosensor applications. In this regard, the importance of generating CNT–NP heterostructures, in terms of various interactions, has been discussed,[18] including noncovalent interactions that exploit the conversion of sp^2-hybridized carbon atoms on CNT surfaces to their sp^3-hybridized analogues to introduce defect sites, electrostatic interactions that exploit charged polymer-coated CNT surface interactions with charged NPs, and hydrophobic interactions that exploit functionalized NP and CNT interactions. The resulting nanocomposites have found applications in sensors, including the voltammetric determination of colorants in foods using Fe_3O_4@SiO_2/MWCNTs,[28] an IgE biosensor to diagnose cancer cells using MWCNT–AuNP,[29] a humidity sensor using Fe_2O_3/Au/CNTs,[30] chemiresistive sensors for detecting exhaled breath VOCs for cancer diagnosis,[31–33] and optical or electrochemical sensors for biomolecules.[34–37] A study of noncovalent interactions between CNTs and AuNPs recently took the effects of solvent dielectric constant and temperature on controlled assembly of superstructures into consideration,[38] showing that repulsive electrostatic interactions in high dielectric solutions reduced the adsorption of nanoparticles on CNTs, yielding an apparent activation barrier to adsorption (E_a = 9.6 kJ mol^{-1}) within the range expected for noncovalent interactions. A study of van der Waals interactions between MWCNTs and citrate-capped AuNPs[39] showed that changes in the geometric parameters of components had a pronounced effect on CNT nanoparticle affinity, with larger, more polarizable nanostructures exhibiting stronger attractive interactions. Therefore, the ability to control these interactions is important for the exploration of the nanostructural functional properties. The strong tendency of pristine CNTs to aggregate or bundle is inherently associated with large attractive forces. Surface modification of CNTs by functional groups is a common pathway to achieving functional-group-anchored nanoparticles.[40] Monolayer-capped metal nanoparticles have well-defined interparticle spatial properties due to weak hydrophobic interactions.[41] For nanoparticles on CNTs, the tendency of pristine CNTs to aggregate or bundle is reduced and a skeleton-type structure can be created to increase accessibility to large nanostructured surface areas and effective mass transport. Importantly, the coupling of nanoparticles to CNT surfaces can impart the nanotubes with tunable electrical conductivity.

In this report, we demonstrate the intriguing effect of nanoscale curvature on the chemiresistive properties induced by embedding CNTs as the substrate in a molecularly-linked assembly of gold nanoparticles (AuNPs), which can be exploited as sensing interfaces for VOCs. In previous studies on the semiconducting properties of CNTs for sensing applications,[42–44] the small curvature radius feature of CNTs on which nanoparticle assemblies are formed in CNT-based nanocomposites has not been explored. In previous studies,[42–44] we showed that the electrical properties of a thin-film assembly of gold nanoparticles on a chemiresistor with flexible PET (polyethylene terephthalate) substrate depended on the curvature radius (R_b) of the PET substrate caused by changes in interparticle distances (from d_1 at R_{b1} to d_2 at R_{b2}). Under these conditions, the ratio of resistances (R) before and after the change in curvature radius can be expressed using eqn (1):[44]

$$\frac{R_t}{R_i} = \exp[-\beta(d_1 - d_2)] \exp\left[\frac{0.5e^2}{4\pi\varepsilon\varepsilon_0 RT}\left(\frac{1}{r+d_1} - \frac{1}{r+d_2}\right)\right] \quad (1)$$

where the resistance changes from R_i to R_t with changes in interparticle distance of d_1 to d_2, β is the electron coupling term, r is the particle core radius, and ε is dielectric constant of the interparticle medium. Other parameters, and relative changes in terms of $\Delta R/R_i$, are given in the ESI.† The R_t to R_i ratio contains two exponential components, the first mainly determined by change in interparticle distance and the β value ("β–d term"), and the second largely dependent on particle size, interparticle distance change, and ε value ("ε–r term"). Our recent studies on flexible PET chemiresistors coated with nanoparticle thin-film assemblies showed that film resistance responded to PET device strain (compressive or tensile strain).[44] For tensile strain, with respect to nanoparticle assembly on the nanoscale-curved CNTs regardless of the microscale device strain, the logarithm of R_t/R_i ($\ln(R_t/R_i)$) was a function of the curvature radius (R_b). For the nanoparticle assemblies on CNTs studied in this work, nanoscale radius curvature played an important role in the β–d term. Fig. 1a compares the effects of radius curvature on relative electrical resistance in nanoparticle assemblies on nanoscale and bulk-scale substrates. As shown by the plots of $\ln(R_t/R_i)$ *vs.* R_b for nanoparticle thin films on CNT and PET substrates (Fig. 1b and c, respectively), which are based on eqn (1), $\ln(R_t/R_i)$ increases when R_b decreases, and decreases with increasing ε. A five-fold increase in $\ln(R_t/R_i)$ is observed when R_b is reduced by a factor of 15 in the bulk-scale R_b range (Fig. 1c, insert; mm range). In comparison, there is a 20–100-fold increase in $\ln(R_t/R_i)$ when R_b is reduced by a factor of 15 in the nanoscale range (Fig. 1b, insert). Both the "β–d" and "ε–r" terms play important roles in determining response characteristics as a function of R_b. With very small R_b, which corresponds with the CNT case, the dominant role of the "β–d term" leads us to the hypothesis that the chemiresistive characteristics of the nanoparticle thin-film assembly on the nanoscale-curved CNTs, in response to perturbations in the interparticle properties, would differ from that on a planar substrate (with an infinitive curvature radius).[44–46]

While the $\ln(R_t/R_i)$ *vs.* ε plots at a fixed R_b (13 nm and 13 mm) show similar overall percentage changes in R_t/R_i in the plotted ranges (84% for nanoscale and 92% for bulk-scale), the absolute values of R_t/R_i are markedly different, demonstrating that ε has a much greater impact on the increase in electrical resistance of the nanoscale-curved substrate than the bulk-scale curved substrate. Therefore, under nanoscale-curve con-

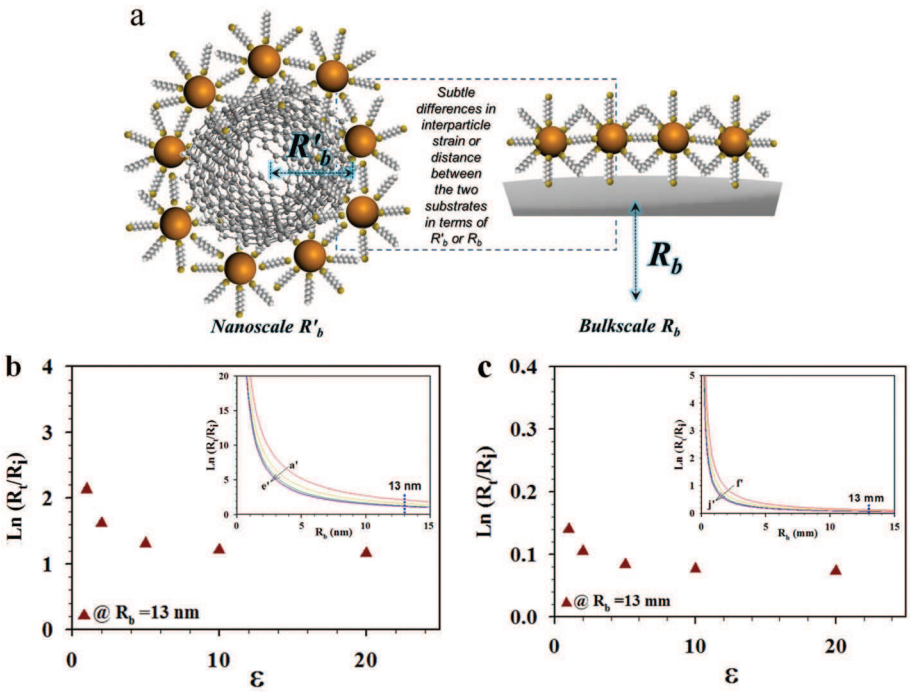

Fig. 1 (a) Comparison of the effect of curvature radius (R_b) on changes in relative resistance in nanoscale and bulk-scale substrates. Plots of $\ln(R_t/R_i)$ *vs.* ε extracted from $\ln(R_t/R_i)$ *vs.* R_b plots at (b) 13 nm and (c) 13 mm (inserts) based on eqn (1), in terms of tensile strain for AuNP assemblies on CNT (b; thickness, ~2 nm) or PET (c; thickness, 125 μm) with different ε values (1 (a′ and f′), 2 (b′ and g′), 5 (c′ and h′), 10 (d′ and i′), and 20 (e′ and j′)).

ditions, the dominant increase in electrical resistance upon exposure to vapors of different dielectric properties (leading to a change in interparticle dielectric medium properties of the nanoparticle assembly) may override changes caused by other factors. It should be noted that the interparticle properties, not the curvature radius of the CNTs, change during vapor exposure. Simulations in Fig. 1 illustrate the differences in the electrical properties of nanoparticle assemblies containing nanoscale-curved and bulk-scale bent substrates (at a fixed curvature radius in each case) in response to changes in dielectric medium properties.

In this study, using monolayer-protected Au nanoparticles on CNTs assembled by exchange-crosslinking-precipitation[47,48] as a model for nanocomposite thin films, we demonstrate the unique effect of nanoscale curvature on chemiresistive sensing properties, showing the influence of the CNT nanoscale-curvature-induced changes on the film response characteristics to VOC sorption. The films also feature skeleton-type structures for effective surface area amplification.

2. Experimental section

2.1 Chemicals

1,9-Nonanedithiol (NDT) and decanethiolate (DT) were used as received (Aldrich). Multiwalled carbon nanotubes (MWCNTs; diameter, ~26 nm) with a purity of ~95% were obtained from NanoLab (Brighton, MA). Polystyrene (PS, Aldrich) and dichloromethane (CH_2Cl_2, 99.9%, Fisher) were used as received. Vapors were generated from hexane (99.9%, Fisher), toluene (99.8%, Fisher), methanol (MeOH, 99.9%, Aldrich), ethanol (EtOH, 99.9%, Aldrich), 1-propanol (PrOH, 100%, J.T. Baker), and 1-butanol (BuOH, 99.9%, J. T. Baker).

2.2 Synthesis and preparation

Compared with DT or other thiolate-capped AuNPs, NDT-linked AuNPs have better stability due to interparticle linkage.[45] AuNPs with a core size of 2 nm encapsulated with DT monolayer shells were synthesized using a two-phase method[49] and a synthetic modification.[50] Details of the synthesis of 2 nm gold nanoparticles (Au_{nm}, 1.8–2.1 nm) have been described previously.[16] Nanoparticle assembly involved suspending CNTs and gold nanoparticles in a controlled ratio in hexane, to which NDT was added as a linking molecule in a controlled concentration. The CNT surface was first treated with concentrated hydrochloric acid to remove surface oxides. After treatment, the CNTs were dispersed in hexane by sonication. Typical concentrations were 16 μM for Au_{nm}, and 0.37 mg mL^{-1} for CNTs. After stirring for ~10 h, the powder was collected, rinsed thoroughly with solvent, and dried under ambient conditions before further characterization.

2.3 Characterization and sensor measurement

A Hitachi H-7000 Electron Microscope (100 kV) was used for transmission electron microscopy (TEM) analysis of the nanomaterials. The samples were first suspended in hexane, then drop cast onto a carbon-coated copper grid, and dried by solvent evaporation under ambient conditions.

Sensor responses were measured using a customized sensor array testing station. The interdigitated microelectrode (IME), featuring 300 pairs of platinum electrodes (length, 50 μm; width, 5 μm) with 5 μm spacing on a glass substrate (100 nm thick), was used as the chemiresistor device. The thickness of the nanocomposite film was less than or similar to the microelectrode thickness. Sensor coating preparation involved suspending (NDT-Au_{nm})/CNT powder into a solution of polystyrene/CH_2Cl_2 (0.01 g mL^{-1}), which was then cast onto the IME surface in a controlled quantity, followed by solvent evaporation under ambient conditions. Polystyrene (PS) acted as a fixation agent. The (NDT-Au_{nm})/CNT-coated sensor was denoted as (NDT-Au_{nm})/CNTs/IME, whereas the NDT-Au_{nm} coated sensor was denoted as (NDT-Au_{nm})/IME. A computer-interfaced multi-channel electrical multimeter (Keithley) was used to measure the resistance of the nanostructured coating on the IME device in a Teflon chamber (2 × 2 × 2 cm^3) with vapor-tubing connections. The resistance (R) was reported as the relative differential resistance change ($\Delta R/R_i$, where ΔR represents the resistance response, and R_i represents the initial resistance). Vapor generation was carried out using a standard protocol, with flowmeters controlling the flow rates and mixing ratios.[45] Vapor concentrations (in ppm (M)) were determined from the partial vapor pressure and vapor mixing ratio, which was converted to ppm (V) by multiplying by 24.5. Details of the experimental measurement procedures were described in earlier reports.[51]

3. Results and discussion

3.1 Interparticle spatial properties and interactions

Molecularly-mediated thin-film assemblies of gold nanoparticles have been prepared by a simple exchanging-cross-linking-precipitation route on planar substrates,[47] carbon spheres, and CNTs.[16] As an interparticle linker, 1,9-nonanedithiol (NDT) forms covalent-type bonds with the gold surface at both ends of the dithiol.[16,47] FTIR analysis of NDT-linked Au_{nm} on CNTs revealed the presence of predominant CH_2 stretching bands and the near-absence of CH_3 stretching bands, consistent with the assembly of NDT-Au nanoparticles on planar gold surfaces.[16] AuNP coverage on the CNTs was controlled by adjusting the relative concentrations of AuNPs, CNTs, and NDTs. Example morphologies of NDT-linked assemblies of Au_{nm} particles on CNTs obtained with controlled ratios of NDTs, AuNPs, and CNTs are shown in Fig. 2. While the general morphology was similar to those previously reported,[16] the spatially isolated feature revealed some details regarding interparticle distances. The nanoparticle assembly was not aligned in any specific direction relative to nanotube diameter or length, and the packing density of the assembled nanoparticles increased with increasing relative concentration of [Au_{nm}] *vs.* [CNT]. As described earlier,[16] the packing density was ~2 × 10^{12} particles per cm^2 with an average diameter of 26 nm for CNTs, which was smaller than that of NDT-linked Au_{nm} particles in ideal close-packing on planar surfaces (~10 × 10^{12} particles per cm^2). A higher concentration led to a higher packing density or multiple layers. An estimate of the density of the Au_{nm}–CNT nanocomposite (~1.5 g cm^{-3}, see ESI†) indicated that coating the CNT with a monolayer of DT-$Au_{2\ nm}$ nanoparticles did not change the density significantly, in comparison with the density of carbon nanotubes (~1.3 g cm^{-3} (ref. 52)). Notably, the film thickness depended on assembly conditions. In this work, we focused on films assembled under the same conditions to compare the sensing properties.

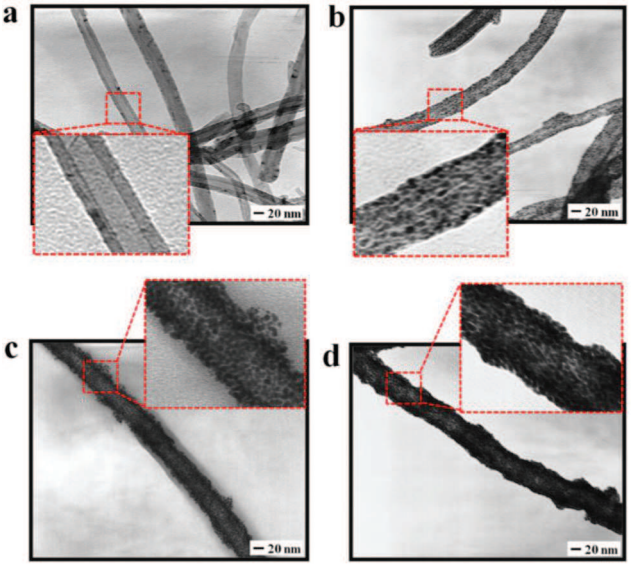

Fig. 2 TEM micrographs of (a) CNTs, and (b–d) (NDT-Au_{nm})/CNTs derived under three different assembly conditions: [NP]/[NDT] ratio fixed at 2.1 × 10^3, while [NP(mM)]/[CNTs(mg mL^{-1})] ratios are 24 (b), 48 (c), and 110 (d).

As a linker molecule, NDT also played an important role in defining the interparticle spatial properties of the assembled AuNPs. In control experiments carried out in the absence of linker molecules, the image of the same nanoparticle sample showed the presence of loosely-scattered particles on both CNT and carbon films in the TEM grid. The average nearest-neighbor interparticle center-to-center or edge-to-edge distances were measured using the TEM data (Fig. 3), which revealed subtle differences among decanethiolate (DT)-Au_{nm} particles (a, top), NDT-Au_{nm} particles on planar carbon in the TEM grid (a, bottom), and NDT-Au_{nm} particles on CNTs (b). TEM analysis allowed the determination of average interparticle center-to-center or edge-to-edge distances (Table S1†). For the DT-Au_{nm} film (Fig. 3a, top), an average interparticle edge-to-edge distance of 1.8 ± 0.3 nm was obtained, which was quite consistent with expectations based on a model of interdigitation of alkyl thiolates on shells between neighboring nanoparticles.[41] For the NDT-Au_{nm} film (Fig. 3a, bottom), the average interparticle distance was 1.5 ± 0.5 nm. For (NDT-Au_{nm})/CNT (Fig. 3b), an average interparticle edge-to-edge distance of 2.9 ± 0.7 nm was obtained. The interparticle distance for (NDT-Au_{nm})/CNT was larger than that of NDT-Au_{nm} film on a planar substrate. Nanoparticle assembly

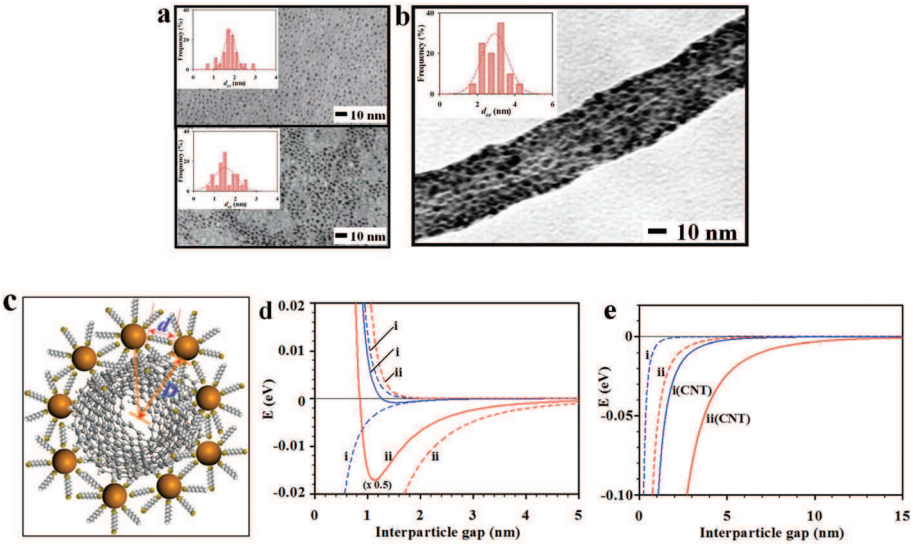

Fig. 3 (a–b) TEM micrographs and interparticle edge-to-edge distances (d_{ee}) for DT-Au_{nm} (a, top panel; d_{ee}, ~1.8 ± 0.3 nm), NDT-Au (2 nm) on planar carbon film in the TEM grid (a, bottom panel; d_{ee}, ~1.5 ± 0.5 nm), and NDT-Au_{nm} on CNTs (b; d_{ee}, ~2.9 ± 0.7 nm). (c) Model for calculation of NP–CNT and NP–NP interactions (AuNPs (2 nm) with CNTs (26 nm)) in terms of interparticle gap (d or D). (d) Calculated steric repulsion, van der Waals attraction potentials, and their sum for AuNP–AuNP (2 nm, i) and AuNP–AuNP (6 nm, ii) interactions as a function of interparticle edge-to-edge gap. (e) Calculated van der Waals attraction potentials of (DT-$Au_{2\ nm}$)/$CNTs_{26\ nm}$ (i(CNT)), (DT-$Au_{6\ nm}$)/$CNTs_{26\ nm}$ (ii(CNT)) compared with those of AuNP–AuNP (2 nm, i), and AuNP–AuNP (6 nm, ii) as functions of the interparticle edge-to-edge gap. (Hamaker constant (A) for AuNP–NP (2 nm): 0.8476 eV;[53] and AuNP–CNT: 60 × 10^{-20} J (3.75 eV)[54]). Note that other parameters, δ and σ, representing the length and diameter of a capping molecule on the nanoparticle surface (δ = 0.57 nm, and σ = 0.36 nm for 2 nm AuNPs and 0.40 nm for 6 nm AuNPs), were extracted from data in a previous report.[55]

along the curved nanotubes was evident from the TEM data (Fig. 3b and S1†). Notably, the average interparticle edge-to-edge distance of larger AuNPs (5–6 nm) assembled on CNTs (2.0 ± 0.5 nm, see Fig. S1†) was smaller than that of 2 nm-sized nanoparticles on CNTs, which was consistent with the expected interparticle gap based on steric repulsion and van der Waals attraction, as discussed below.

Therefore, the curvature radius of the nanotube affects interparticle interactions. A major adhesive force responsible for nanoparticle assembly on the CNT surface involves van der Waals interactions between the organic shell and carbon surface. This type of adhesion is apparently quite strong, as evidenced by the particles not being easily removed by extensive washing and sonication, as supported by TEM characterization. Theoretically, steric repulsion and van der Waals attraction operate in particle–particle and the particle–CNT interactions (Fig. 3c). Fig. 3d and e show the calculated interaction potentials for these two models (see ESI† for details). There are clear differences in interparticle gaps and interaction potentials between the particle–particle and particle–CNT interactions. As shown in Table 1, comparisons of interparticle edge-to-edge gaps for NDT-assembled AuNPs of two different sizes (2 nm and 6 nm) on flat C film and curved CNT (measured from TEM) and the interaction-minimum-derived interparticle gaps (obtained from calculations of steric repulsion and van der Waals attraction) resulted in several significant observations: (1) the interparticle distance was greater for NPs assembled on the curved CNT than on the flat C film; (2) larger-sized particles exhibited smaller gaps for both flat and curved substrates; and (3) the interaction was stronger for AuNP–CNT than AuNP–AuNP pairs. These observations were in agreement with the assessment of the effect of nanoscale curvature on interparticle interactions and distances. Notably, particle–CNT strong adhesion was supported by the experimental observation that removing particles from CNTs was

Table 1 Interparticle edge-to-edge gaps for NDT-assembled AuNPs on flat C film and curved CNT measured using TEM data, and interaction-minimum-derived interparticle gaps from calculations of steric repulsion and van der Waals attraction

Particle size	TEM gap (C film)	TEM gap (CNT)	Calc'd gap[a]	Calc'd attraction/CNT[b]
Au (2 nm)	1.5 ± 0.5 nm	2.9 ± 0.7 nm	1.5 nm	0.7 nm
Au (6 nm)	1.3 ± 0.4 nm	2.0 ± 0.5 nm	1.1 nm	0.6 nm

[a] Model: symmetric dimer of AuNPs. Hamaker constant (A) for AuNP–NP (2 nm): 0.8476 eV and for AuNP–NP (6 nm): 0.8407 eV;[53] δ and σ stand for the length and diameter of a capping molecule on the nanoparticle surface, δ (0.57 nm) and σ (0.36 nm for 2 nm AuNPs, and 0.40 nm for 6 nm AuNPs), were obtained from the reported data and the following equation (ratio of the surface occupied by a thiol molecule on a NP (σ_R) and on a flat surface (σ_F): $\frac{\sigma_R}{\sigma_F} \propto \frac{s_R}{s_F} = \frac{1}{1+d/R}$, ($\sigma_F$ = 0.14 nm^2).[55] For $Au_{2\ nm}$, σ_R/σ_F = 0.17, the diameter of a capping molecule on the nanoparticle surface is 0.36 nm. For $Au_{6\ nm}$, σ_R/σ_F = 0.88, the diameter of a capping molecule on the nanoparticle surface is 0.40 nm. [b] Model: asymmetric dimer of AuNP and CNT ((DT-$Au_{2\ nm}$)/$CNT_{26\ nm}$ and (DT-$Au_{6\ nm}$)/$CNT_{26\ nm}$). Hamaker constant (A) for AuNP–CNT: 60 × 10^{-20} J (3.7452 eV).[54] The length and diameter of a capping molecule on the nanoparticle surface (δ and σ) are the same as in (a).

difficult, and substantiated by the interparticle potential energy calculation (see Fig. 3). This inherent strong adhesion was not from polystyrene, which only helped fix the overall composite film to the chemiresistor surface.

NP–CNT interaction was much stronger than the NP–NP interaction, as reflected in the smaller interparticle gap and larger potential for NP–CNT interaction. This was consistent with the experimental observation that NP adhesion to CNTs was favored, whereas the NP–NP interactions were weak in the absence of NDT linkage. The combination of interparticle NDT linkage and the NP–CNT strong attractive interactions led to AuNP assembly on the CNT surface. This type of interparticle interaction was exploited to harness the chemiresistive sensing properties. Notably, the morphologies have a subtle influence on the VOC response sensitivities because of the subtle differences in interparticle spatial properties.[45,56] Given that the three assembly conditions have little influence on films obtained with the same thickness, the VOC response measurements described below focus on films prepared under the same conditions.

3.2 Nanoscale curvature induced changes in sensing properties

The combination of nanoscale-curvature-tuned interparticle spatial properties and skeleton-type nanoparticle–CNT nanocomposites on interdigitated microelectrode (IME) as a chemiresistor was expected to enhance the electrical properties, VOC accessibility and mass transport characteristics of the nanocomposite structure. Bare MWCNTs, upon casting on an IME, were electrically conductive or semiconductive because of good electronic contacts between the conductive CNTs. However, the electronic conductivity of DT-capped Au particles coated on CNTs was dependent on both electronic contact properties at particle–CNT or particle–particle interfaces and the electronic conductivity of the composite ensemble. The change in electronic properties due to interfacial interactions constitutes a basis for designing sensing materials responsive to vapor sorption in the nanostructure. Electrical conductivity is determined by the particle size, interparticle distance, and dielectric medium properties of the nanoparticle–CNT composite materials, and is, therefore, expected to respond to the quantity and chemical or physical nature of the vapor molecules being adsorbed into the nanostructure. We focused on demonstrating the viability of the nanoparticle–CNT composites as enhanced sensing materials, in comparison with nanoparticle sensing materials without CNTs, by investigating the response properties to volatile organic compounds (VOCs).

The measured resistance values of the thin-film scaffolds on the IME devices were compared to assess the relative conductivities (Fig. S2†). First, the comparison was made under the assumption that the film thickness was the same for all films. Compared with the values for polystyrene (PS)/CNTs/IME, the conductivities of both PS/(NDT-Au_{nm})/CNTs/IME and PS/(NDT-Au_{nm})/IME were at least 3–4 orders of magnitude smaller. The conductivity of PS/(NDT-Au_{nm})/CNTs/IME were around one order of magnitude smaller than that of PS/(NDT-Au_{nm})/IME. This result demonstrated that the electrical conductivities of PS/(NDT-Au_{nm})/CNTs/IME and PS/(NDT-Au_{nm})/IME were dominated by the nanoparticle assembly, not the CNTs. Given that the CNT was coated with a monolayer of DT-$Au_{2\ nm}$ nanoparticles, that the electrical conductivity was largely dictated by the nanoparticle assembly, and that the estimated density of the Au_{nm}–CNT nanocomposite remained similar to that of the CNTs (see ESI†), it was believed that CNT largely functioned as a fibrous skeleton substrate for nanoparticle assembly. Notably, the actual thickness of the PS/(NDT-Au_{nm})/CNTs/IME was at least 5–10 times greater than that of PS/(NDT-Au_{nm})/IME. The polymer did not influence the electrical conductivity of the nanocomposites, and functioned only as a binder for the nanoparticle-coated CNTs, enabling their fixation as a thin-film scaffold to the interdigitated microelectrode device.

The relative differential resistance change ($\Delta R/R_i$, where ΔR is the resistance response and R_i is the initial resistance) of the nanocomposite on the IME device in response to toluene and hexane vapor was measured (see Fig. S3†). Polystyrene thin film (<100 nm) was used to increase the mechanical strength of the coating materials on the IME surface, at which the sensor response displayed a minimum level of noise. With the absence of polymer, the data were less reproducible due to the likelihood of the movement of nanotubes in the coating, especially under repeated vapor sorption–desorption cycles. Because of the possible effect of added polymeric materials on sensing response, we also included control experimental data, namely the response data for polystyrene-coated CNTs/IME, obtained under identical conditions for comparison. Compared with the control, which showed no response (Fig. S3a,† curve-b′) because the semiconducting characteristic was not operative when the CNT surface was coated with the nanoparticle assembly, (NDT-Au_{nm})/CNTs/IME (curve-a′ in Fig. S3a†) showed clear response profiles upon exposure to different concentrations of toluene vapor. In general, the (NDT-Au_{nm})/CNT coating on IME had resistance in the order of ~30 MΩ, which was much greater than that of a simple CNT coating on IME (~1 kΩ). This difference was qualitatively consistent with the presence of nanoparticles and the polymer in the nanocomposite material. Similar response profiles were observed for hexane vapor (Fig. S3b†), which showed a subtle difference in response sensitivity.

The observation that (NDT-Au_{nm})/CNT is responsive to vapor sorption shows that molecular partition and interaction in the nanocomposite scaffold can be effectively converted to a change in electrical conductivity *via* the embedded nanotubes. The detected resistance change displays a positive response profile, with a decrease in electronic conductivity of the coating as a result of partition of the vapor analyte into the nanostructure.[45] In the control experiment, the use of CNTs or polystyrene/CNTs (curve-b′) alone as coating materials produced no response due to the lack of change in electronic conductivity. The plots of $\Delta R/R_i$ *vs.* vapor concentration (moles per liter, ppm) display a good linear relationship (Fig. S3† insert). The slope measures the response sensitivity dependent on

both the nature of the vapor molecule and the structural properties of the sensing materials, as reflected in the response to toluene being more sensitive to that of hexane.

Remarkably, completely different responses were observed using methanol (MeOH) vapor with (NDT-Au_{nm})/CNTs/IME and (NDT-Au_{nm})/IME. In Fig. 4, the response profiles for the sorption of MeOH vapors to (NDT-Au_{nm})/CNTs/IME (a′) and (NDT-Au_{nm})/IME (b′) are compared. Positive responses were observed for (NDT-Au_{nm})/CNTs/IME (a′), in contrast to the negative responses for (NDT-Au_{nm})/IME (b′). In addition, the positive responses for (NDT-Au_{nm})/CNTs/IME clearly increased with MeOH vapor concentration, whereas the negative responses for (NDT-Au_{nm})/IME showed no clear trend as the MeOH vapor concentration was changed. This sharp contrast was believed to reflect the operation of the small curvature radius in (NDT-Au_{nm})/CNTs. As shown in Fig. 1, the "β–d term" played a dominant role in changing the electrical properties of (NDT-Au_{nm})/CNTs/IME. This was different from (NDT-Au_{nm})/IME, where both "β–d" and "ε–r" terms played important roles in determining the response characteristics as a function of R_b, often yielding negative responses from the adsorption of vapors with high dielectric constants, a phenomenon observed in our previous work[45] and by others.[46] To our knowledge, this is the first example of the same NDT-AuNPs assembly demonstrating different response profiles using different supporting substrates. Notably, interparticle interactions, as illustrated in Fig. 3d and e, are important for tuning the vapor–film interactions responsible for the vapor sensing properties.

While CNTs function as a fibrous skeleton substrate for the assembly of nanoparticles, the open structure could not be attributed to the absence of negative response to methanol. The intriguing response characteristics were further explored using alcohol molecules of different chain lengths. In Fig. 5, the response profiles of (NDT-Au_{nm})/CNTs/IME to the sorption of different alcohol (R–OH) vapors are compared. In addition to the common hydrophilic –OH groups, these vapors (methanol (MeOH, a), ethanol (EtOH, b), 1-propanol (PrOH, c), and 1-butanol (BuOH, d)) contain different hydrophobic R groups (size: MeOH < EtOH < PrOH < BuOH). The dielectric constants of these molecules decreased in the order MeOH (ε = 33.0) > EtOH (ε = 25.3) > PrOH (ε = 20.8) > BuOH (ε = 17.8). The plot of $\Delta R/R_i$ *vs.* vapor concentration displayed good linearity (Fig. 5, right), with the slope used to measure response sensitivity. The response profiles and response sensitivities for (NDT-Au_{nm})/IME were also measured in response to the same series of alcohol vapors (MeOH, EtOH, PrOH, and BuOH) (see Fig. S4a†). In comparison with the response profiles for (NDT-Au_{nm})/CNT/IME (Fig. 5), there were two distinct differences. Firstly, (NDT-Au_{nm})/IME exhibited both negative and positive response profiles depending on the chain length of the alcohol vapors (Fig. S4a†), and secondly, the slopes (Fig. S4b†) were significantly smaller than those of (NDT-Au_{nm})/CNT/IME. These results suggested that the sensing properties were profoundly affected by the presence of nanotubes.

A close examination of the detailed response profiles provided important information for assessing the sensing properties. In the absence of CNTs (Fig. S4†), the response profile was negative for MeOH (a′), but positive for BuOH (d′). For EtOH (c′) and PrOH (d′), the small and spiky response profiles appeared to be a mixture of these two extremes. A negative response indicated an increase in electrical conductivity as a result of the partition of vapor molecules in the sensing film, whereas a positive response showed a decrease in electrical conductivity.[45] The intermittent spiky responses suggested the involvement of both behaviors in a relatively dynamic way. Although similar behavior has been observed for similarly nanostructured films on a 15 μm-spaced IME device,[45] the observation of these negative or negative-to-positive response profiles at the 5 μm-spaced IME device was remarkable, demonstrating that the IME gap size played a role in amplifying response characteristics. A larger gap[45] shows a response between positive and negative, whereas a smaller gap (as in this study) features mainly a negative response to methanol.[57] We also performed repetitive runs to examine sensor reproducibility. In most cases, the response profiles were repeatable, except for EtOH and PrOH vapors with (NDT-Au_{nm})/IME (Fig. S4†), for which the second run, as shown by the dashed lines (Fig. S4a,† pink curves), showed subtle changes in response profile. In general, this change was a transition from a negative to positive response profile, but the overall response magnitude was small. This dynamic nature was indicative of vapor-induced structural changes in the NDT-Au_{nm} film.

In comparison with sensor responses for NDT-Au_{nm} sensing films (see Fig. S4†), which exhibited a detection limit of ~20 ppb for the VOCs,[51] the noise levels in the response curves for (NDT-Au_{nm})/CNTs films were larger by a factor of ~8, making the detection limit lower in the present work. This likely reflected the loose packing of the nanoparticle-coated CNTs on the IME substrate. This problem could be addressed by thin-film processing, such as annealing or preconditioning, of the nanocomposite films, which is part of our ongoing work.

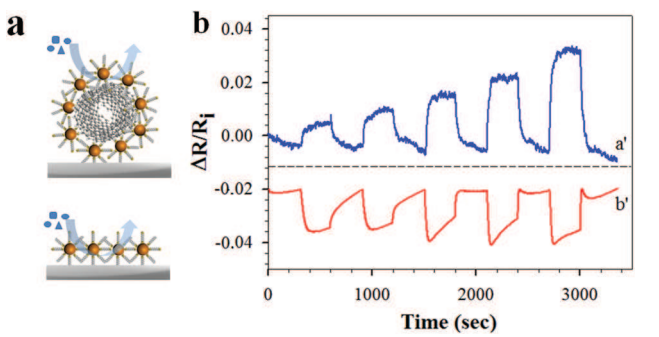

Fig. 4 (a) Illustration of vapor sorption at the two different types of nanoparticle thin-film interfaces. (b) Response profiles for methanol vapor (vapor concentrations: 347, 694, 1389, 2083, and 2777 ppm (M)), comparing (NDT-Au_{nm})/CNTs/IME (a′) and (NDT-Au_{nm})/IME (b′), as illustrated in the left panel (a).

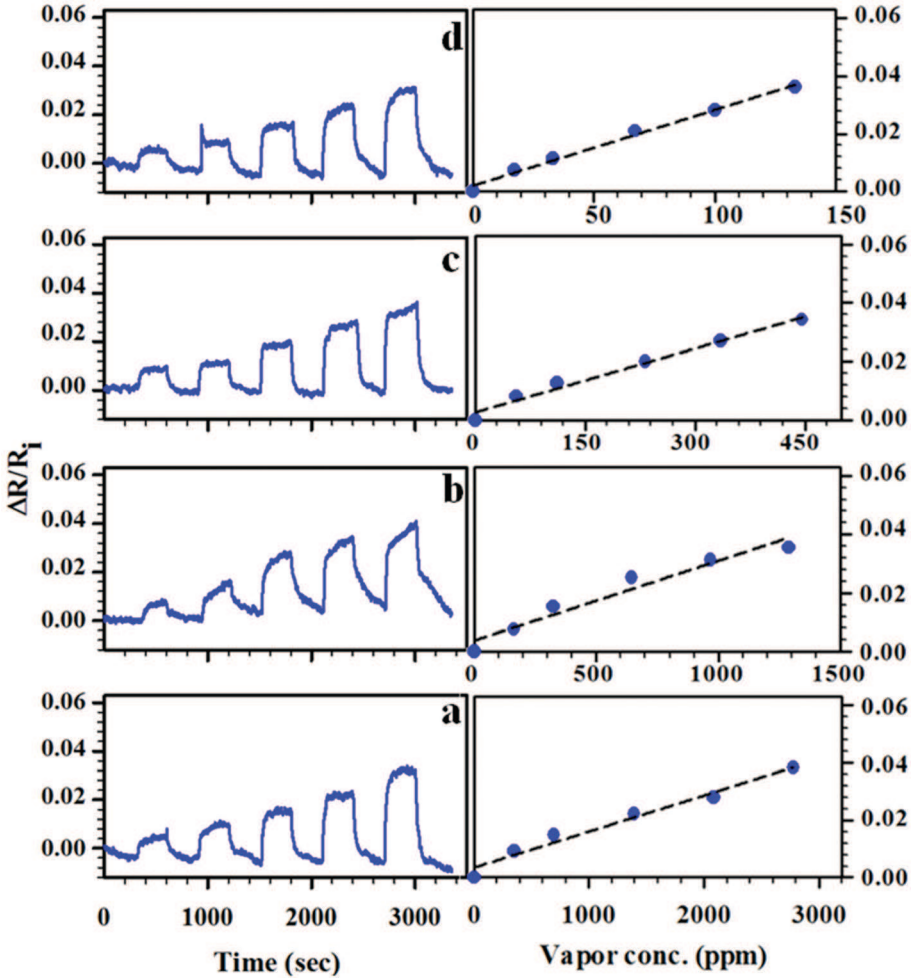

Fig. 5 Response profiles of (NDT-Au_{nm})/CNTs/IME using different R–OH vapors (MeOH (a) vapor concentrations: 347, 694, 1389, 2083, 2777 (in ppm (M)), EtOH (b) vapor concentrations: 161, 322, 644, 966, 1288 (in ppm (M)), PrOH (c) vapor concentrations: 56, 112, 232, 335, 446 (in ppm (M)) and BuOH (d) vapor concentrations: 17, 33, 67, 100, 133 (in ppm (M))). Right: Plots of response *vs.* concentration of different R–OH vapors (in ppm (M)) at (NDT-Au_{nm})/CNTs/IME (linear regression slopes: 1.3×10^{-5} (MeOH), 2.7×10^{-5} (EtOH), 7.3×10^{-5} (PrOH), 2.6×10^{-4} (BuOH)).

The sharp distinction of response profiles for different alcohol vapors between (NDT-Au_{nm})/CNTs/IME (Fig. 5) and (NDT-Au_{nm})/IME (Fig. S4†) is that the former displays a consistent positive response profile, regardless of the size of the alkyl group and the dielectric constant of the vapors. In addition to increased dielectric properties for the shorter-chain alcohols affecting electron hopping between nanoparticles, the sharp contrast was believed to reflect changes in electrical properties due to the combination of hydrophobic monolayer-capped AuNPs and the unique surface characteristics of CNTs with effective mass transport within the nanostructure. Furthermore, the small curvature radius of the CNTs was believed to play a dominant role in dictating the response profile, as shown earlier in eqn (1) and Fig. 1, where the "β–d term" was able to override the "ε–r term" for a small curvature radius.

For CNTs fully coated with nanoparticles, the average interparticle distances of all particles in relation to the nanoscale curvature effect should be the same, regardless of the relative orientation of the nanotubes on the microelectrode substrate. Since electrical conductivity was determined by the nanoparticle assembly, not by the CNTs, the change in electrical conductivity of the nanoparticle assembly on the nanoscale-curved CNTs to a perturbation of the interparticle properties by the adsorption of VOCs should be the same for all nanoparticles coated on the CNT surface. As such, the origin of the negative response profiles for the nanoparticle assembly on CNTs with respect to direct nanoparticle assembly on the microelectrode substrate could be mainly attributed to the nanoscale curvature effect, as defined by the interparticle distance changes in relation to changes in the curvature-dependent electrical properties (see eqn (1)).

To understand the correlation between the nanostructure and the sensing properties, the above assessments were further substantiated by comparing response sensitivities using different alcohol vapors for both (NDT-Au_{nm})/CNTs/IME and (NDT-Au_{nm})/IME. Both displayed clear increasing trends in the order MeOH < EtOH < PrOH < BuOH, while the response magnitude was greater for the nanoparticle–nano-

tube composite film (Fig. 6). The enhanced accessibility of the CNT-regulated interparticle voids played an important role in determining the response properties of the nanostructure. The response sensitivities were ordered by increasing hydrophobic R group size in R–OH, exhibiting an exponential increase relative to the number of carbons in the alcohol molecules (Fig. 6a, insert). Remarkably, the sensitivity (S) was described by a simple exponential relationship with chain length (N, the chain C number, $S = a \times e^{bN}$, where a and b are constants). Interestingly, this trend coincided with the trend in terms of Hansen solubility parameter (∂_t) (see Fig. 6b), which is defined as[58]

$$\partial_t = \sqrt{\partial_d{}^2 + \partial_p{}^2 + \partial_h{}^2} \quad (2)$$

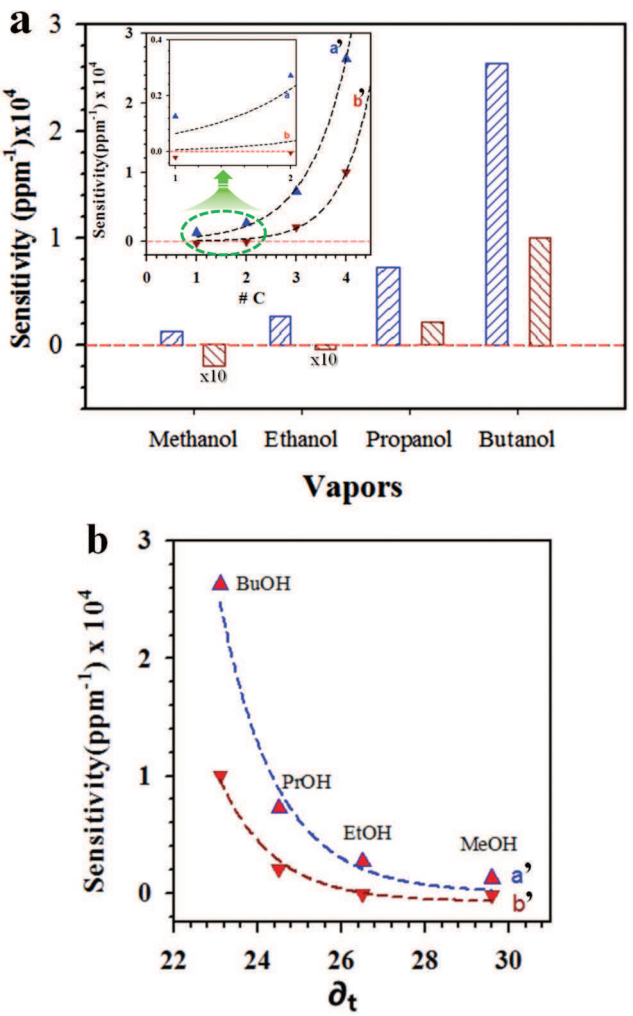

Fig. 6 (a) Response sensitivities of (NDT-Au_{nm})/CNTs/IME (blue bars) and (NDT-Au_{nm})/IME (red bars) in response to exposure to a series of alcohols. Insert: Plots of response sensitivity *vs.* number of carbons in R–OH (#C). Data are fitted by an exponential growth model yielding: (a') $y = 1.92 \times 10^{-2}\, e^{1.23x}$ ((NDT-Au_{nm})/CNTs/IME) and (b') $y = 1.34 \times 10^{-3}\, e^{1.65x}$ ((NDT-Au_{nm})/IME). (b) Plots of response sensitivity *vs.* total solubility parameter: ((a') (NDT-Au_{nm})/CNTs/IME) and (b') ((NDT-Au_{nm})/IME). (See also Fig. S5† for dependencies on individual parameters in total solubility parameter, and the dielectric constant of the vapor molecules.)

where ∂_d is the dispersion component, ∂_p is the polar component, and ∂_h is the hydrogen bonding component. VOC-induced swelling of polymer materials has been shown to increase when the total solubility parameter decreases.[58] Notably, the solubility parameter is related to thermodynamic activity, which has been widely demonstrated to correlate with VOC sensing data.[59,60] Based on the dependencies of the total solubility parameter and the dielectric constant of the alcohol vapor molecules on individual components (Fig. S5†), the combination of polarity and dispersion components appeared to have a dominant effect on the observed trend. This result again supported the enhanced accessibility of the nanostructure to the VOCs and the operation of hydrophobic interactions inside the nanocomposite framework. Differences in terms of response profiles for shorter chain alcohols and fitting parameters for the data between (NDT-Au_{nm})/CNTs/IME and (NDT-Au_{nm})/IME reflect the significant role played by CNTs in the nanostructure.

As an additional probe of hydrophobicity and polarity characteristics of nanocomposite-sensing properties, data for both (NDT-Au_{nm})/CNTs/IME and (NDT-Au_{nm})/IME, in response to several hydrophobic vapor molecules with different substitutions, including benzene, toluene, and xylenes, were also compared (see Fig. S6a†). VOCs, such as benzene, toluene, and xylene, are major air toxins or pollutants, resulting from various emission sources. Excessive exposure to benzene can be harmful to the immune system, and adverse health effects caused by VOC exposure have received public attention. For these hydrophobic VOCs, the sensing responses all give positive profiles. The response sensitivity showed a clear increasing trend with methyl-group substitution on the aromatic ring (Fig. S6a† insert). As shown in Fig. S6b,† this trend was consistent with the total solubility parameter trend. Considering the dependencies on individual components in the total solubility parameter (Fig. S7†), the dispersion component appeared to be dominant in the observed trend.

In general, the amount of NDT-Au_{nm} particles directly assembled on the IME device was much greater than that on (NDT-Au_{nm})/CNTs/IME. This was caused by differences in packing density and mass loading of the assembled nanoparticles, as determined by TEM and QCM (quartz crystal microbalance) analyses. For (NDT-Au_{nm})/IME, the assembled particles were in 57 equivalent layers, while for (NDT-Au_{nm})/CNTs/IME, the assembled particles were $\leq$1 equivalent layer. In general, the response sensitivity for (NDT-Au_{nm})/CNTs/IME was greater than that of (NDT-Au_{nm})/IME. This greater response sensitivity for (NDT-Au_{nm})/CNTs/IME reflected the effective accessibility of the large surface areas on the nanocomposite structures to analytes. Nanoparticle loading on (NDT-Au_{nm})/IME was ~50 times larger than that on (NDT-Au_{nm})/CNTs/IME. This increased response sensitivity for nanoparticle–nanotube composite materials was again suggestive of enhanced accessibility of the nanostructured surfaces to the analyte, and the unique conductive property of the nanocomposite. These findings again demonstrate that the formation of nanoparticle–nanotube composites provides intri-

guing tunability of the interparticle spatial properties to influence the electrical properties relative to direct use of a nanoparticle assembly. It should be noted that the response profiles were complex, depending on a combination of factors. For this reason, we focused on a system of 2 nm particles for a more detailed understanding. A further study with different particle sizes is ongoing. Further investigations are needed to establish quantitative correlations between nanocomposite structures and sensitivity, selectivity, response times, and detection limits for a range of VOCs.

4. Conclusions

This study has demonstrated the viability of highly sensitive detection of VOCs using nanoscale-curvature-induced changes in chemiresistive properties in molecularly-linked assemblies of gold nanoparticles on multiwalled carbon nanotubes. The electrical properties tuned by the nanoscale curvature radius of the nanotubes enabled consistent positive response profiles to VOCs, which were distinct from nanoparticle thin-film assemblies on planar substrates. The dominant effect of electron coupling on the overall chemiresistive properties was shown in relation to the nanoscale curvature radius, which correlated well with VOC solubility parameters. The enhanced sensing properties also benefitted from increased accessibility of VOCs to the nanostructured interface. The consistent positive response profile, regardless of alkyl group size and dielectric constant of the vapors, reflected the dominant role played by the "β–d term" in the electrical properties of the thin-film assembly with a small curvature radius. Moreover, the correlation of response sensitivity with alcohol vapor molecule size or aromatic vapor molecule substitution coincided with the trend in total solubility parameter, which demonstrated the importance of hydrophobicity and polarity based interactions on nanocomposite sensor response characteristics. In addition to the quantitative correlation of these molecular interactions in terms of selectivity, response time, and detection limit, studies of the nanoscale curvature correlation with CNTs of different diameters and other similarly shaped nanomaterials are part of future work, with the aim to gain insight into the design of highly sensitive sensor interfaces for the detection of VOCs from various sources, including air pollutants for emission control and human breath for health monitoring.

Acknowledgements

This work was supported by the National Science Foundation (IIP 1640669) and the Shanghai Sailing Program (16YF1411400).

References

1 S. I. Lim and C. J. Zhong, *Acc. Chem. Res.*, 2009, **42**, 798–808.
2 L. Wang, J. Luo, M. J. Schadt and C. J. Zhong, *Langmuir*, 2010, **26**, 618–632.
3 C. Farcau, N. M. Sangeetha, H. Moreira, B. Viallet, J. Grisolia, D. Ciuculescu-Pradines and L. Ressier, *ACS Nano*, 2011, **5**, 7137–7143.
4 N. M. Sangeetha, N. Decorde, B. Viallet, G. Viau and L. Ressier, *J. Phys. Chem. C*, 2013, **117**, 1935–1940.
5 E. Palleau, N. M. Sangeetha, G. Viau, J. D. Marty and L. Ressier, *ACS Nano*, 2011, **5**, 4228–4235.
6 M. Segev-Bar and H. Haick, *ACS Nano*, 2013, **7**, 8366–8378.
7 G. Konvalina and H. Haick, *Acc. Chem. Res.*, 2014, **47**, 66–76.
8 G. Peng, U. Tisch, O. Adams, M. Hakim, N. Shehada, Y. Y. Broza, S. Billan, R. Abdah-Bortnyak, A. Kuten and H. Haick, *Nat. Nanotechnol.*, 2009, **10**, 669–673.
9 G. Peng, E. Trock and H. Haick, *Nano Lett.*, 2008, **8**, 3631–3635.
10 M. Hakim, Y. Y. Broza, O. Barash, N. Peled, M. Phillips, A. Amann and H. Haick, *Chem. Rev.*, 2012, **112**, 5949–5966.
11 M. Segev-Bar, A. Landman, M. Nir-Shapira, G. Shuster and H. Haick, *ACS Appl. Mater. Interfaces*, 2013, **5**, 5531–5541.
12 A. Amann, B. Costello, W. Miekisch and T. Risby, *J. Breath Res.*, 2014, **8**, 034001.
13 P. Rai, R. Khan, S. Raj, S. M. Majhi, K. K. Park, Y. T. Yu, I. H. Lee and P. K. Sekhar, *Nanoscale*, 2014, **6**, 581–588.
14 D. Matatagui, O. V. Kolokoltsev, N. Qureshi, E. V. Mejía-Uriartea and J. M. Saniger, *Nanoscale*, 2015, **7**, 9607–9613.
15 J. J. Xu, W. W. Zhao, S. P. Song, C. H. Fan and H. Y. Chen, *Chem. Soc. Rev.*, 2014, **43**, 1601–1611.
16 L. Han, W. Wu, F. L. Kirk, J. Luo, M. M. Maye, N. Kariuki, Y. Lin, C. Wang and C. J. Zhong, *Langmuir*, 2004, **20**, 6019–6025.
17 S. N. L. Wulan and B. Yuliarto, *J. Electrochem. Soc.*, 2016, **163**, 97–106.
18 X. H. Peng, J. Y. Chen, J. A. Misewich and S. S. Wong, *Chem. Soc. Rev.*, 2009, **38**, 1076–1098.
19 A. La Torre, M. D. Gimenez-Lopez, M. W. Fay, C. H. Lucas, P. D. Brown and A. N. Khlobystov, *Small*, 2015, **11**, 2756–2761.
20 X. H. Pham, C. A. Li, K. N. Han, B. C. Huynh-Nguyen, T. H. Le, E. Ko, J. H. Kim and G. H. Seong, *Sens. Actuators, B*, 2014, **193**, 815–822.
21 A. M. Ashrafi, S. Cerovac, S. Mudric, V. Guzsvany, L. Husakova, I. Urbanova and K. Vytras, *Sens. Actuators, B*, 2014, **191**, 320–325.
22 Y. F. Zhang, C. L. Xu, B. X. Li and Y. B. Li, *Biosens. Bioelectron.*, 2013, **43**, 205–210.
23 S. Shahrokhian and S. Rastgar, *Analyst*, 2012, **137**, 2706–2715.
24 Y. X. Fang, S. J. Guo, C. Z. Zhu, S. J. Dong and E. K. Wang, *Chem. – Asian J.*, 2010, **5**, 1838–1845.
25 F. H. Li, Z. H. Wang, C. S. Shan, J. F. Song, D. X. Han and L. Niu, *Biosens. Bioelectron.*, 2009, **24**, 1765–1770.
26 J. Zhang, G. Wang, Y. S. Shon, O. Zhou, R. Superfine and R. W. Murray, *J. Phys. Chem. B*, 2003, **107**, 3726–3732.

27 C. Tasaltin and F. Basarir, *Sens. Actuators, B*, 2014, **194**, 173–179.
28 M. Arvand, Y. Parhizi and S. H. Mirfathi, *Food Anal. Methods*, 2016, **9**, 863–875.
29 H. Y. Li, J. Wu, J. M. Melnyczuk, O. Olubi, L. I. Lewis, Y. Cao, P. Nagappan, S. A. Khan, C. W. Ingram and I. I. Harruna, *J. Nanosci. Nanotechnol.*, 2015, **15**, 5733–5740.
30 J. Lee, S. Mulmi, V. Thangadurai and S. S. Park, *ACS Appl. Mater. Interfaces*, 2015, **7**, 15506–15513.
31 R. M. Shereema, S. R. Nambiar, S. S. Shankar and T. P. Rao, *Anal. Methods*, 2015, **7**, 4912–4918.
32 B. Singh, N. Bhardwaj, V. K. Jain and V. Bhatia, *Sens. Actuators, A*, 2014, **220**, 126–133.
33 X. H. Sun, K. Shao and T. Wang, *Anal. Bioanal. Chem.*, 2016, **408**, 2759–2780.
34 N. Yusoff, A. Pandikumar, R. Ramaraj, H. N. Lim and N. M. Huang, *Microchim. Acta*, 2015, **182**, 2091–2114.
35 S. Kumar, W. Ahlawat, R. Kumar and N. Dilbaghi, *Biosens. Bioelectron.*, 2015, **70**, 498–503.
36 C. Yang, M. E. Denno, P. Pyakurel and B. J. Venton, *Anal. Chim. Acta*, 2015, **887**, 17–37.
37 F. R. Baptista, S. A. Belhout, S. Giordani and S. J. Quinn, *Chem. Soc. Rev.*, 2015, **44**, 4433–4453.
38 G. A. Rance and A. N. Khlobystov, *Dalton Trans.*, 2014, **43**, 7400–7406.
39 G. A. Rance, D. H. Marsh, S. J. Bourne, T. J. Reade and A. N. Khlobystov, *ACS Nano*, 2010, **4**, 4920–4928.
40 J. Kong, N. R. Franklin, C. Zhou, M. G. Chapline, S. Peng, K. Cho and H. Dai, *Science*, 2000, **287**, 622–625.
41 L. Han, J. Luo, N. Kariuki, M. M. Maye, V. W. Jones and C. J. Zhong, *Chem. Mater.*, 2003, **15**, 29–37.
42 W. Zhao, J. Luo, S. Shan, J. P. Lombardi, Y. Xu, K. Cartwright, S. Lu, M. Poliks and C. J. Zhong, *Small*, 2015, **35**, 4509–4516.
43 S. Shan, W. Zhao, J. Luo, J. Yin, J. C. Switzer, P. Joeseph, S. Lu, M. Poliks and C. J. Zhong, *J. Mater. Chem. C*, 2014, **2**, 1893–1903.
44 J. Yin, P. Hu, J. Luo, L. Wang, M. F. Cohen and C. J. Zhong, *ACS Nano*, 2011, **5**, 6516–6526.
45 L. Han, D. R. Daniel, M. M. Maye and C. J. Zhong, *Anal. Chem.*, 2001, **73**, 4441–4449.
46 E. García-Berríos, T. Gao, M. D. Woodka, S. Maldonado, B. S. Brunschwig, M. W. Ellsworth and N. S. Lewis, *J. Phys. Chem. C*, 2010, **114**, 21914–21920.
47 L. Han, M. M. Maye, F. L. Leibowitz, N. K. Ly and C. J. Zhong, *J. Mater. Chem.*, 2001, **11**, 1258–1264.
48 M. J. Hostetler, C. Templeton and R. W. Murray, *Langmuir*, 1999, **15**, 3782–3789.
49 M. Brust, M. Walker, D. Bethell, D. J. Schiffrin and R. Whyman, *J. Chem. Soc., Chem. Commun.*, 1994, **7**, 801–802.
50 M. J. Hostetler, J. E. Wingate, C. J. Zhong, J. E. Harris, R. W. Vachet, M. R. Clark, J. D. Londono, S. J. Green, J. J. Stokes, G. D. Wignall, G. L. Glish, M. D. Porter, N. D. Evans and R. W. Murray, *Langmuir*, 1998, **14**, 17–30.
51 L. Han, X. Shi, W. Wu, F. L. Kirk, J. Luo, L. Wang, D. Mott, L. Cousineau, S. I. Lim, S. Lu and C. J. Zhong, *Sens. Actuators, B*, 2005, **106**, 431–441.
52 P. G. Collins and P. Avouris, *Sci. Am.*, 2000, **283**, 62–69.
53 P. Pinchuk and K. Jiang, *Proc. SPIE*, 2015, **9549**, 95491J.
54 A. Weddemann, I. Ennen, A. Regtmeier, C. Albon, A. Wolff, K. Eckstädt, N. Mill, M. K.-H. Peter, J. Mattay, C. Plattner, N. Sewald and A. Hütten, *Beilstein J. Nanotechnol.*, 2010, **1**, 75–93.
55 A. Jiménez, A. Sarsa, M. Blázquez and T. Pineda, *J. Phys. Chem. C*, 2010, **114**, 21309–21314.
56 L. Wang, X. Wang, J. Luo, B. N. Wanjala, C. Wang, N. Chernova, M. H. Engelhard, I.-T. Bae, Y. Liu and C. J. Zhong, *J. Am. Chem. Soc.*, 2010, **132**, 17686–17689.
57 J. H. Luo, J. Luo, L. Wang, X. Shi, J. Yin, E. Crew, S. Lu, L. M. Lesperance and C. J. Zhong, *Sens. Actuators, B*, 2012, **161**, 845–854.
58 C. M. Hansen, *Hansen solubility parameter: a user's hand book*, Florida, CRC Press, 2000.
59 M. C. Lonergan, E. J. Severin, B. J. Doleman, S. A. Beaber, R. H. Grubbs and N. S. Lewis, *Chem. Mater.*, 1996, **8**, 2298–2312.
60 M. P. Eastman, R. C. Hughes, G. Yelton, A. J. Ricco, S. V. Patel and M. W. Jenkins, *J. Electrochem. Soc.*, 1999, **146**, 3907–3913.